Rheological control on the segmentation of the mid-ocean ridges: Laboratory experiments with extension initially perpendicular to the axis

A.L.R. L R Sibrant, A. Davaille, E. Mittelstaedt

Rheological control on the segmentation of the mid-ocean ridges. Part 1: laboratory experiments with extension initially perpendicular to the axis

A.L.R. Sibrant[a,b,c], A. Davaille[a,*], E. Mittelstaedt[b,a]

[a] *Laboratoire FAST (CNRS / Univ. Paris-Sud), Bat.530-Pascal, Rue Andre Riviere, Campus Universitaire, 91 405 ORSAY cedex, France.*
[b] *Department of Geological Sciences, University of Idaho, Moscow, Idaho, USA.*
[c] *Univ Brest, CNRS, IUEM, UMR6538, Geosciences Ocean, F-29290 Plouzane, France*

Abstract

Mid-ocean ridges (MOR) axes are not straight, but segmented over scales of 10s to 100s of kilometers by several types of offsets including transform faults (TF), overlapping spreading centers (OSC) and non-transform, non-overlapping offsets (NTNOO). Variations in axial morphology and segmentation have been attributed to changes in magma supply, axial thermal structure (which depends on mantle temperature and spreading rate), and axial mechanical properties. To isolate the effect of each of these processes is difficult with field data alone. We therefore present a series of analogue experiments using colloidal silica dispersions as an Earth analogue. Diffusion of salt from saline solutions placed in contact with these fluids, cause formation of a skin, whose rheology evolves from viscous to elastic and brittle with increasing salinity. Applying a fixed spreading rate to this pre-formed, brittle plate results in cracks, faults, and ridge segments. Lithospheric thickness is varied independently by changing the surface water layer salinity. Experimental results depend on the axial failure parameter Π_F , the ratio of a mechanical length scale (Z_m) and the axial elastic thickness (Z_{axis}), which depends on mantle temperature and spreading velocity. Slow-spreading fault-dominated, and fast-spreading fluid intrusion-dominated, ridges on Earth and in the laboratory are separated by the same critical value $\Pi_{Fc}\pm 0.024$, suggesting that the axial failure mode governs ridge geometry. Here, we examine ridge axis segmentation. Measurements of >4000 experimental ridge segments and offsets yield an average segment length L_m that is quasi-constant at all spreading velocities. Scaled to the Earth, L_m ∼55 km, in agreement with the natural data. Experiments with low Π_F show offset size varying as $d_l = cste\sqrt{L_m Z_{axis}}$ regardless of offset type, a correlation well explained by fracture mechanics. Finally, as on Earth, experimental ridge segments are separated by transform and non-transform discontinuities, and their nature and occurrence vary with Π_F. NTNOOs develop when $\Pi_F < \Pi_{Fc}$, while OSCs develop when $\Pi_F > \Pi_{Fc}$. In contrast, TF may form at any Π_F, but the proportion of TFs relative to OSCs or NTNOOs decreases when $\Pi_F/\Pi_{Fc} >> 1$ or $<< 1$, in agreement with natural MOR.

Keywords: mid-ocean ridge, segmentation, axial mechanical strength, laboratory experiments, transform faults

1. Introduction

Segmentation of spreading ridges is a global fundamental phenomenon which highlights the three-dimensional process of crustal accretion (MacDonald, 1982; Whitehead et al., 1984; Schouten et al., 1985). High-resolution bathymetric mapping reveals changes in mid-ocean ridges continuity and linearity, which subdivide the ridges into spreading segments (Hey, 1977; Schouten and Klitgord, 1982). These segments are disrupted by offsets (fig.1) such as transform faults (TF), and non-transform fault structures including overlapping spreading centres (OSC), zero-offset transform faults (ZoT), or deviations in axial linearity ($devals$) (Schouten and Klitgord, 1982; Wilson, 1965; Schouten and White, 1980; MacDonald and Fox, 1983; Lonsdale, 1983; Langmuir et al., 1986; Bosworth, 1986; Schouten

*davaille@fast.u-psud.fr

et al., 1987).

Spatial variations in magmatic accretion and tectonic deformation control the evolution of the oceanic lithosphere and can lead to systematic variations in mid-ocean ridge segmentation and faulting (e.g. Phipps Morgan et al. (1987); Buck et al. (2005); Howell et al. (2019)). Segmentation should therefore strongly depend on spreading rate and on magma supply. Early observations at fast- and intermediate-spreading ridges (e.g. Lonsdale (1983); Cochran and Sempere (1997)) suggested that a large magma flux lead to small lateral offsets (typically from 3 to 30 km, with outliers up to 140 km; Macdonald et al. (1988)) of the axis between long spreading segments (65 to 145 km in length; Schouten et al. (1985); MacDonald and Fox (1992)). In contrast, slow-spreading and some intermediate-spreading ridges reported to have lower magma fluxes (Schouten et al. (1985); Sandwell (1986)), larger lateral offsets (range from 3 to 100 km, up to 900 km; Sempere et al. (1993); Bonatti et al. (1994)), and shorter spreading segments (50 km in length; Schouten et al. (1985)). However, a more recent compilation of bathymetric, geochemical and geophysical observations from the last 30 years, reveals a quasi-regular length scale of ridge segmentation (30 to 50 km on average) at all spreading rates (Carbotte et al. (2015)).

The dynamic evolution of mid-ocean ridge segmentation is commonly discussed with respect to spreading rate. Indeed, spreading rate exerts a first-order control on both the rate of deformation and the thermal structure of the plate boundary. Yet, there are numerous anomalous spreading centers, such as the Reykjanes Ridge and the Australian Antarctic Discordance, with axial morphologies and melt supplies that differ from ridges with similar spreading rates. The structure and evolution of these anomalous ridges not only depend on spreading rate but also on mantle temperature and melt supply (Ito et al. (1999); Sempere et al. (1991)). Moreover, both magmatic (through dikes) and tectonic (through faults) styles of accretion are governed by the mechanics of the lithosphere and therefore its mechanical and rheological properties (Buck et al. (2005); Chen and Morgan (1190); Howell et al. (2019)). Based on experimental modelling, we recently suggested that the mode of axial failure (tectonic or magmatic) and the overall shape of oceanic ridges depend on a single parameter, the axial failure parameter Π_F. Π_F is the ratio of a length scale that only depends on the mechanical properties of the plate boundary, and the axial elastic thickness which depends on mantle temperature and spreading velocity (Sibrant et al. (2018)). Here, we extend our previous study to the segmentation characteristics and offset types of mid-ocean ridges. We limit our investigation to cases of constant, symmetric spreading velocity initially perpendicular to the spreading axis. To avoid biases that may be present in statistics on natural data due to the uneven distribution of plate velocities and mantle temperature (fig.2), our laboratory experiments allow the collection of statistics on the equivalent of a 15,000 km-long MOR for each spreading velocity and mantle temperature considered.

2. Laboratory experiments

2.1. Setup and visualization

The experimental setup consists of a Plexiglas tank (33 x 23 x 6 cm high) partially filled with Ludox, a colloidal silica dispersion, and covered by a saline solution (fig.3A). Chemical diffusion of salt into the Ludox triggers the formation of a white skin at the interface between the two liquids. This skin is a two-phase material composed at the 10-100 nm-scale of a silica skeleton with an interstitial brine. The skin initially forms just above and subsequently adheres to two horizontal plates driven by an electric motor applying a constant, divergent velocity. The two horizontal plates are initially separated by a thin, vertical barrier to enforce two initially separate gelled zones; the vertical barrier is removed just prior to the onset of spreading. During each experiment, the plates move at a constant and uniform velocity (full spreading rate V between 2 and 20 mm/min) causing fractures to nucleate at the center of the experimental tank. In addition to passive upwelling of Ludox due to the diverging motion of the plates (Houseman (1983); Gerya (2010)), the less dense Ludox can also rise by buoyancy within the denser and salted fractured skin. The rising Ludox forms a gel when it enters in contact with the downward-diffusing salt.

The top surface of each experiment is illuminated with a white light to follow the evolution of the spreading axis. The surface configuration was captured every 3-7 seconds with a Nikon camera equipped with a 200mm zoom (4288 x 2848 pixels; 0.109 mm per pixel) through an oblique mirror (45^o) place above the tank. Uncertainties in spatial measurements are estimated at three times the pixel

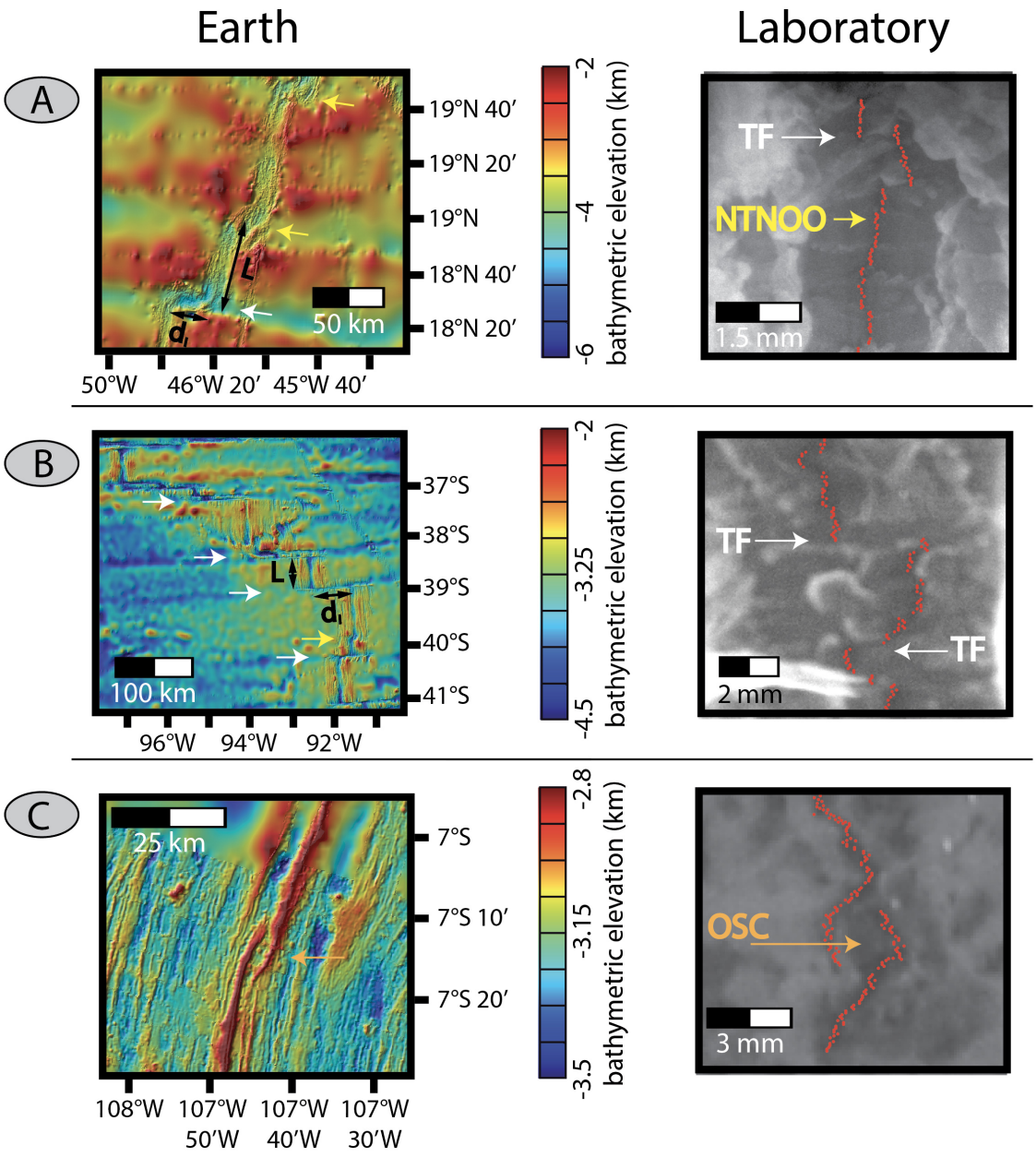

Figure 1: Zoology of discontinuities observed on Earth (left panels) and reproduced in the laboratory (right panels) including examples of non-transform non-overlapping offset, NTNOO, see text (A), transform fault, TF (B) and overlapping spreading centre, OSC (C). The small red dots indicate the axis location determined by the image local intensity minima.

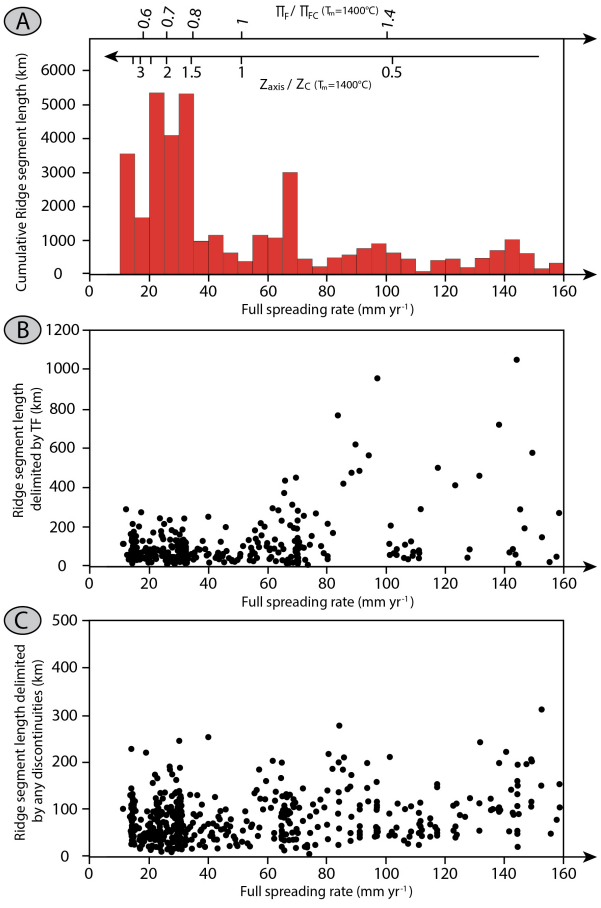

Figure 2: Histograms of natural data: (A) total length of MOR accreted at a given spreading velocity; (B) distance between two successive TFs; (C) distance between two successive offsets of any kind.

resolution (i.e., 0.3 mm). In addition, the surface of the fluid is illuminated by ten 635 nm red laser lines placed at a 45^o angle; deflection of these lines on the skin surface allows measurements of the skin topography (Sibrant et al. (2018)). Three experiments were also recorded at 1 Hz with a high-resolution Pixelink(R) camera equipped with a macro zoom (2592 x 1944 pixels; 0.012 mm per pixel) with a 3 cm field of view centered on the spreading axis.

The formation of the experimental skin induced by salt diffusion is analogous to the formation of the oceanic lithosphere by cooling (i.e. thermal diffusion). The axial skin elastic thickness Z_{axis} is controlled by the balance of advection and diffusion and depends on the initial concentration of the saline water ΔC_0 and on the full spreading rate V as (Mjelde et al. (2008)):

$$Z_{axis} = -\frac{2\kappa_C}{V} log(\frac{\Delta C_c}{\Delta C_0/2}) = -\frac{2\kappa_T}{V} log(\frac{T_c - T_m}{T_0 - T_m}) \quad (1)$$

where κ_C and κ_T are the chemical and thermal diffusivity, respectively. On Earth, $T_0 - T_m$ is the temperature contrast between surface and mantle, and T_c is the temperature below which the lithosphere is elastic-brittle (e.g. 650^oC; McKenzie et al. (2005)). In the laboratory, ΔC_c is the critical concentration above which the skin formation is nearly instantaneous (Shih et al. (1999)). The rheology of the skin evolves from viscous to elastic-brittle with increasing salinity. Ludox free of salt shows a Newtonian behavior (Di Giuseppe et al. (2012)). With addition of salt, Ludox exhibits a visco-plastic behavior with an overlying elastic-brittle part (Sibrant and Pauchard (2016)). The elastic-brittle behavior is observed if the NaCl concentration at the interface is greater than the critical concentration ΔC_c=0.48 mol/l (Davaille and Vah, manuscript in preparation). For the salt concentrations between 2.79 and 6.15 mol/l used in this study, the axis of the experimental ridges is always solid. By separately changing the surface saline concentration and plate spreading velocity, analogous to separately changing the mantle temperature or the spreading rate, the experiments cover a large range of spreading velocity and axial lithosphere thickness. Moreover, although there is no melting in the experiments, liquid is always available to rise through the experimental lithosphere and gel. Therefore, this set-up mimicks a situation where melt supply is constant and always present.

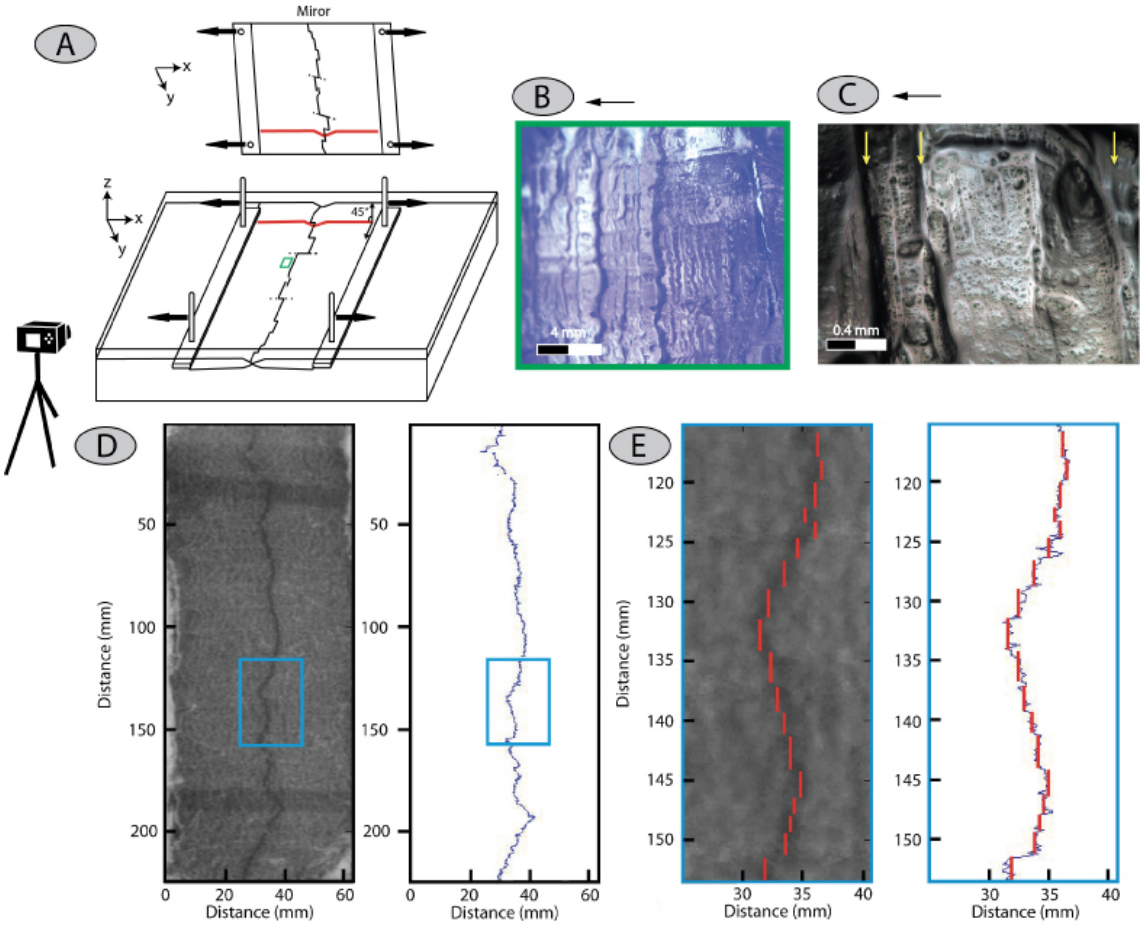

Figure 3: (A) Schematic illustration of the experimental apparatus. (B-E) Top view images. (B) Zoom on the green square shown in (A) for V=1 mm/min and I=6.15 mol/l. (C) Microscope image of the gelled skin for V=20 mm/min and I=4.28 mol/l. The black horizontal arrow indicates how the image moves away from the ridge. Yellow arrows indicate faults which developed perpendicular to the spreading direction along the axis valley. (D) Ridge morphology in the laboratory (for V=10 mm/min, I=4.28 mol/l) and automatically determined ridge axis using Matlab. The blue rectangles indicate the location of the zoom shown in (E). Red lines indicate ridge segments.

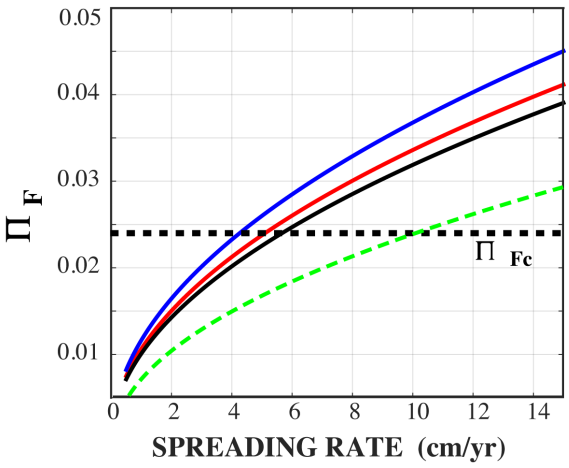

Figure 4: Evolution of Π_F (equation (3)) as a function of spreading velocity for different mantle temperatures and thermal diffusivities. The solid lines are for κ_T=10^{-6} m^2/s; the dashed lines are for κ_T=2.10^{-6} m^2/s. In blue, T_m=1600^{o}C; in red and in green, T_m=1400^{o}C; in black, T_m=1300^{o}C.

2.2. Dimensionless parameters

The physical properties for the laboratory experiments and the axial oceanic lithosphere are given in Table A1. Dynamic similarity of spreading ridges between our analogue model and the Earth is demonstrated using three dimensionless numbers:

The Prandtl number, $Pr = \nu/\kappa$, compares momentum diffusivity, ν (kinematic viscosity of the bulk fluid) to the thermal (for the Earth) or chemical (for the laboratory) diffusivity, κ. A large Pr number ($>> 1$) indicates that the inertial forces are negligible, and the motions stop as soon as their driving force stops. This is the regime prevailing on Earth ($Pr \sim 10^{22}$), as in our experiments ($Pr \sim 10^4$).

Growth of the lithosphere is characterized by the Peclet number which compares advection and diffusion: $Pe = HV/\kappa$, where H is the thickness of the fluid or the asthenosphere and V is the full spreading rate. The large value of Pe ($>> 1$) encountered both on Earth ($Pe = 1300 - 1600$) and in the laboratory ($Pe = 156 - 1562$) ensures that skin/lithosphere formation occurs.

The most important aspects of MOR evolution are characterized by the axial failure parameter, Π_F (Sibrant et al. (2018)). Π_F describes the controls on material deformation and failure and, thus, the behavior of the skin under accretion:

$$\Pi_F = \frac{K_{1c}}{\sigma_Y \sqrt{Z_{axis}}} = \sqrt{\frac{Z_m}{Z_{axis}}}, \tag{2}$$

where K_{1c} is the fracture toughness, σ_Y is the yield stress defining the boundary between plastic (ductile) and elastic-brittle behavior. Π_F depends on the spreading velocity through Z_{axis}, but equation (1) shows that it varies also with mantle temperature and lithosphere thermal diffusivity (fig.4). A higher mantle temperature above a plume will correspond to a higher Π_F value, while an increased effective thermal diffusion (e.g., by hydrothermal circulation) will correspond to a lower Π_F value. $Z_m = (K_{1c}/\sigma_Y)^2$ is interpreted as the characteristic mechanical length scale below which plasticity becomes dominant in fracture processes. When Π_F is larger than a critical value $\Pi_{Fc} = 0.024 \pm 0.002$, accretion is dominated by intrusion of fresh fluid rising from below. While at low Π_F values, plate failure predominantly occurs from the surface downwards. These changes in failure behavior are similar to the relative ratio of tectonic to magmatic accommodation of plate separation by passive stretching and faulting of the lithosphere or through frequent dike injections (Buck et al. (2005)). We showed that Π_F has a key influence on the morphology of mid-ocean ridges (Sibrant et al. (2018)).

Note that Π_{Fc} corresponds to a critical elastic thickness that only depends on the mechanical properties of the material:

$$Z_c = \frac{Z_m}{\Pi_{Fc}^2} \tag{3}$$

For the Earth, we use the fracture toughness and tensile yield strength of the natural lithosphere corresponding to the effective rock mass values provided by Schultz (1993). These values yield a Z_c of 771 $\pm$ 110 m on Earth and to 3.91 $\pm$ 0.5 $\times$ 10^{-5} m in the laboratory. Hereafter, we use Z_c to scale values from the models and the Earth.

We ran a total of 22 experiments with Π_F between 6.17 $\times$ 10^{-3} and 6.76 $\times$ 10^{-2} (Sibrant et al. (2018)). As the range relevant for present-day Earth is $\Pi_F = 1.1 - 4.0 \times 10^{-2}$, we restrict our discussion to the laboratory experiments within this range. Across the remaining 17 experiments, spreading rates (2 to 20 mm/min) and salinities (2.79 to 6.15 mol/l) were varied systematically (Table A2).

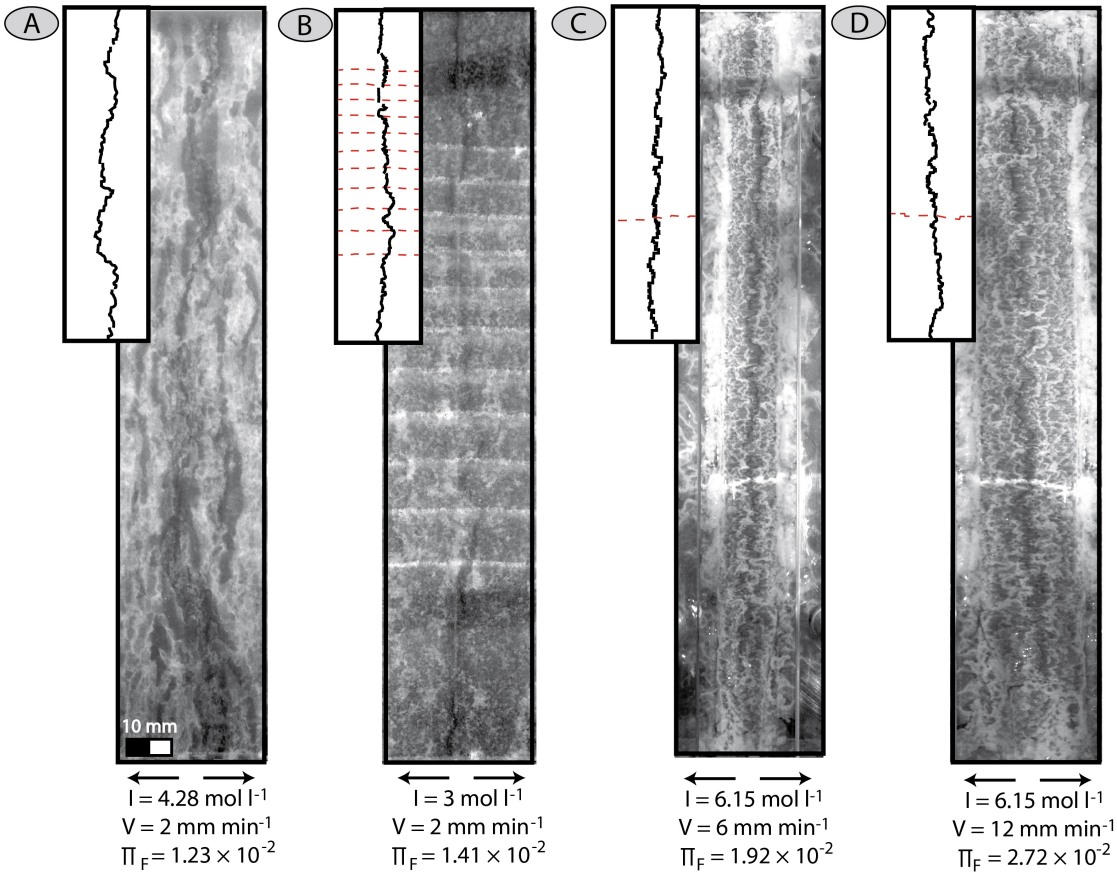

Figure 5: Ridge morphology observed in the experiments for identical spreading velocities and different salinities (A and B), and for identical salinities but different spreading velocities (C and D). Inserts present schematic structural interpretations of the ridge axis (black lines). Red dashed lines indicate the location of the red laser sheets.

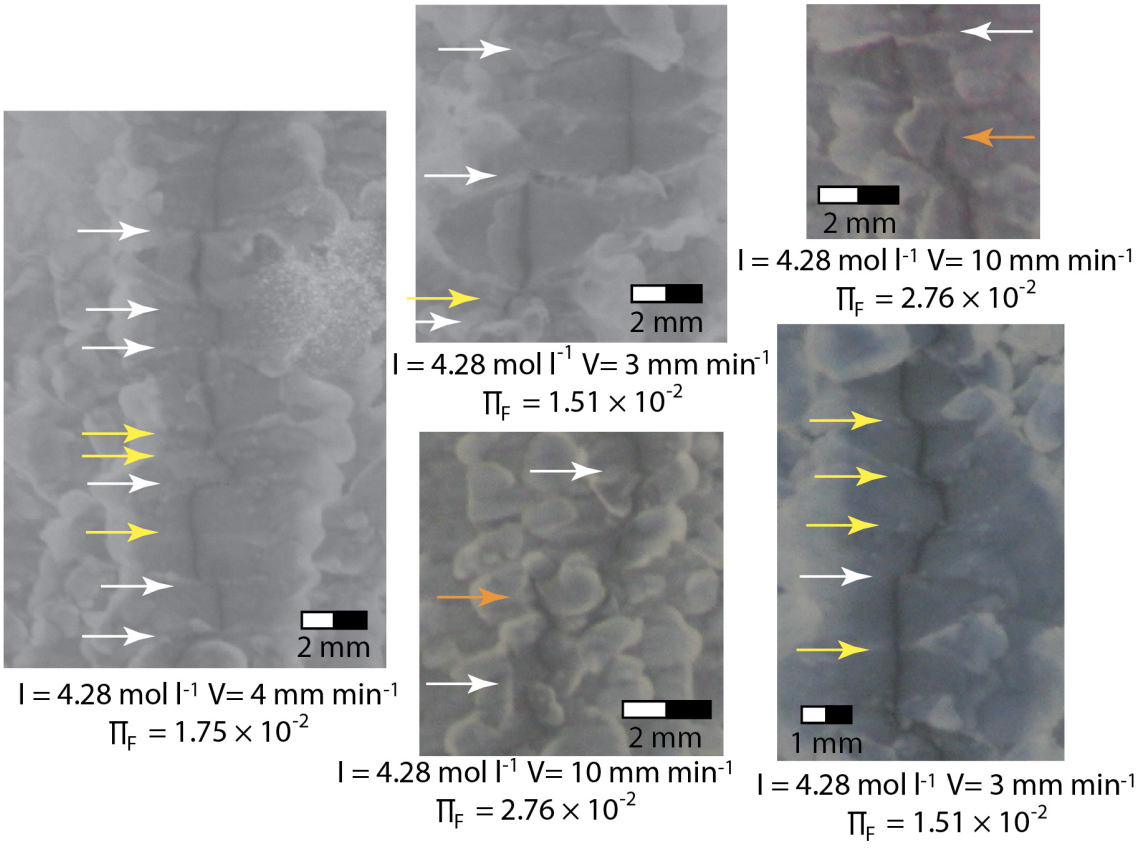

Figure 6: Zoology of the features observed in the laboratory experiments. The arrows indicate transform faults (TF - white), non transform non overlap ridge offsets (NTNOO - yellow) and overlapping spreading centers (OSC - orange).

3. Experimental ridge segmentation

3.1. Measurement method

The location of the axis, and its segmentation, were measured using two methods. On all images, the ridge axis appears darker than the surrounding plates. So the location of the spreading axis was first determined automatically by finding the pixel with minimum intensity along each across-axis row of pixels (fig.3D). However, as inhomogeneous illumination and shadows generated noise, these automatic locations were then used as a guide for manual measurements of each ridge segment length L and lateral offset d_l over the whole 23 cm length of the Plexiglas tank (fig.1 and fig.5). Only ridge segments with length and offset width greater than three times the resolution of the laboratory images (0.1 mm x 3 = 0.3 mm for the Nikon and 0.012 mm x 3 = 0.04 mm using the Pixelink) were included in our analysis. For each experiment, three of these axial profiles were measured after the overall shape of the axis reaches a steady state (see Sibrant et al. (2018)). In total, we measured 4280 segments and 4280 ridge offsets.

Results from the high resolution close up (Pixelink) and from the standard images (Nikon) show consistent results, indicating the robustness of our measurement methods. The type of each ridge offset was determined through careful observations of movies, series of sequential images, and from local PIV velocity fields calculated with an in-house PIV code (fig.1 and fig.3).

3.2. Phenomenology

Our experimental setup ensures that the ridge axis initially is straight (within 0.2 mm) and located in the middle of the tank. During an experiment, the position and geometry of the axis change freely with time (fig.6). In the rest of the paper we use the following definitions to describe features in our experimental results and on Earth:

-A *segment* is defined as an approximately linear zone of spreading, sub-perpendicular (90 ± 15^o) to the plate spreading direction and delimited by two ridge offsets.

-The segments can be offset by *transform faults* which are characterized by major transverse structures (fig.6), striking within 15^o to the spreading direction, with a predominant strike-slip deformation.

-An *overlapping* spreading center is a pair of curved overlapping segment ends showing a hook-shaped geometry (fig.6).

-When tips of an OSC connect to the neighboring segment, the ridge axis surrounds and isolates a piece of lithosphere. This *independent block*, always smaller than 3 mm in the laboratory, can rotate before becoming attached to one side of the ridge. A *microplate* is identified when the angular rotation of an independent block exceeds 90^o. In this case, it becomes visible that the rotating microplate grows by continually accreting young lithosphere and therefore can become larger than 3 mm. As independent blocks and microplates are bounded by several segments and thus by several ridge offset structures, we do not consider these features in this study.

-*Propagating rifts* are defined by a segment that is growing into older crust and is a dynamic evolution of a particular ridge segment instead of another ridge offset type.

-Ridge offsets lacking the narrow zone of spreading-parallel lineaments indicative of localized strike-slip faulting and lacking sufficient overlap between segments (< 0.3 mm) are identified as *non-transform, non-overlapping offsets*, NTNOO (fig.6). On Earth, the NTNOO designation includes structures identified as zero-offset transform faults *ZoT* (Schouten and White (1980)) and deviations from axial linearity *devals* (Langmuir et al. (1986)).

Our experiments (fig.5) show that TF, NTNOO and OSC naturally develop from an initially straight axis: they constitute mechanical instabilities of the accretion axis. Thus, we document the process of segmentation arising from plate accretion instead of inherited from pre-existing weaknesses within the plate.

Development of axial morphology by formation of these mechanical instabilities depends on the spreading velocity and salinity. After a period where the axis increasingly deviates from a straight line due to the accumulation of offsets, every experiment reaches a statistical steady state where the detailed shape of the MOR can change, a given offset can evolve, but the ridge lateral deviation from a straight line remains constant (Sibrant et al. (2018)). So in what follows, we shall focus on the segmentation properties in this steady state. For a given spreading velocity, the steady-state lateral deviation of the axis from a straight line increases with a decrease in salinity (fig.5A,B), creating a more tortuous ridge. For a given salinity, it decreases

with an increase in spreading rate (fig.5C, D), creating a straighter ridge. These morphology variations from a tortuous to straighter ridge correspond to increasing Π_F values (Sibrant et al. (2018)).

3.3. Statistics

Given equations (3)-(4), varying Π_F corresponds to varying the axial lithosphere elastic thickness Z_{axis} compared to Z_C. Therefore, we show results as a function of Z_{axis}/Z_C.

The segment length L is the distance between two consecutive offsets. These offsets can be of any type. Fig.7A shows the distribution of segment lengths for each experiment relative to Z_{axis}/Z_C. The average segment length L_m is approximately constant over the whole Z_{axis}/Z_c range: $L_m = 2.78 \pm 0.14$ mm. Moreover, the maximum segment lengths in each experiment (9.72 - 14.6 mm) are also independent of Z_{axis}/Z_C (Table A3 and fig.A10).

Independently of the ridge offset type (i.e. TF, NTNOO or OSC), the lateral offset of ridges in the direction parallel to spreading motion d_l ranges between 0.3 mm and 5 mm (fig.7B). Within these values, two different trends are visible. When $Z_{axis}/Z_c < 1$, more than 70% of the measurements fall between 0.3 and 1.25 $\pm$ 0.3 mm with an approximately constant mean value: $d_m = 0.57$ mm (fig.7B). When $Z_{axis}/Z_c > 1$, the mean value for each experiment d_l increases with increasing Z_{axis}/Z_c (fig.7B,C). Note that the maximum offset values do not vary over the whole Z_{axis}/Z_c range (fig.7B).

Most ridge offsets measured in the experiments are transform faults (fig.8A). TFs form at all Z_{axis}/Z_c values, i.e. at all spreading rate and salinities, while the development of OSCs and NTNOOs depends on Z_{axis}/Z_c (fig.8B). For $Z_{axis}/Z_c < 1$ (large Π_F, e.g. fast spreading velocities or low salinities), the ridge axis is composed of several segments that may be slightly oblique relative to the perpendicular to the spreading direction, and are separated by OSCs and TFs (fig.6). In contrast, for $Z_{axis}/Z_c > 1$ (e.g. slow spreading rates or high salinities), the ridge axis is composed of a succession of segments perpendicular to spreading and offset by spreading-parallel TFs and NTNOOs (fig.6), but no OSCs are observed.

The number of OSCs and NTNOOs relative to TF depends on Z_{axis}/Z_c (fig.8C). The proportion of OSCs reaches $\sim$20% of the total discontinuities at low Z_{axis}/Z_c and decreases with increasing Z_{axis}/Z_c, until $Z_{axis}/Z_c \sim 1$. NTNOOs then progressively replace OSCs. The occurrence of NTNOOs increases with increasing Z_{axis}/Z_c until reaching $\sim$20% of the discontinuities at the highest Z_{axis}/Z_c. In reflection of the above trends, the proportion of TFs increases up to $Z_{axis}/Z_c \sim 1$, and then decreases.

3.4. Mechanical model to predict the offset size

For $Z_{axis}/Z_c > 1$, fig.7C shows that the ridge lateral offset size increases as a function of Z_{axis}/Z_c. If we suppose that a ridge segment acts as a crack forming as the result of the applied extension (e.g., MacDonald et al. (1991)), this systematic behavior can be explained in the framework of fracture mechanics (Griffith (1924); Allain and Limat (1995); Gauthier et al. (2010)). A crack forms when the internal stress in a material reaches its tensile strength. Then the stress component perpendicular to the crack direction is released in its vicinity. This produces a zone over which no other parallel crack can form. The exact determination of the stress field depends on the mechanical properties of the material. Using the minimum-energy principle, the minimum spacing between two parallel ridge segments is then (Allain and Limat (1995); Gauthier et al. (2010)):

$$d_l = C_e \sqrt{L_G Z_{axis}}, \tag{4}$$

where C_e is an experimental constant which depends on the geometry of the system. The Griffith's length, L_G is:

$$L_G = \frac{K_{1c}^2 (1 - \nu_P^2)}{2\sigma_Y^2} \tag{5}$$

where ν_P is Poisson ratio (Table A1). In the laboratory, $L_G = 1.02 \times 10^{-8}$ m, and the experimental data is well fit by equation (4) for an experimental constant C_e=943.71 (R=0.99195; fig.7C). At $Z_{axis} = Z_c$, this model gives a critical lateral offset value of $d_C = 0.59 \pm 0.07$ mm in close agreement with the experimental measurements (0.57 mm). Note that according to equation (2), (4) can be written as a function of Π_F:

$$d_l = C_e \sqrt{\frac{1 - \nu_P^2}{2}} \Pi_F Z_{axis} \tag{6}$$

or also:

$$d_l = 16.0 \sqrt{(1 - \nu_P^2) Z_c Z_{axis}} \tag{7}$$

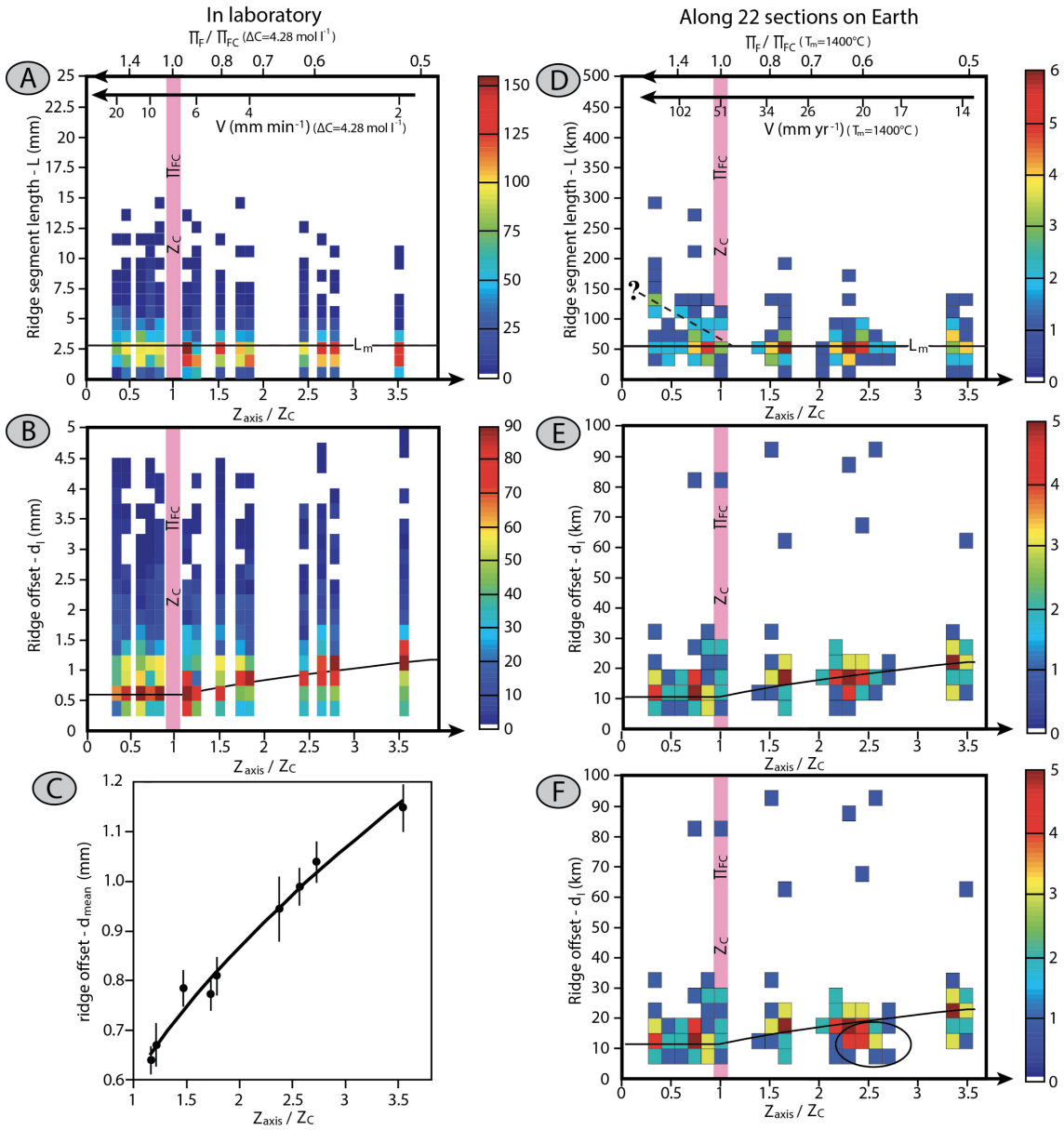

Figure 7: Statistics in (A-C) laboratory experiments and (D-F) natural MOR data (on the 22 MOR sections defined in the text). (A) and (D) Number of segments (in color) as a function of their length L and the local Z_{axis}/Z_c; the solid line indicates the mean L_m value (see fig.A10 and Table A3). On (D) the bin corresponds to 20km for the length and 100 m for Z_{axis}. The dashed line suggests a second trend of segment length for high Π_F. (B) and (E) Number of ridge offsets (in color) as a function of their lateral size d_l and Z_{axis}/Z_c. On (E) the bin corresponds to 5km for d_l and 100 m for Z_{axis}. (C) mean offset size d_l as a function of the Z_{axis}/Z_c. The solid line on (B) and (C) indicates the fit by equation (5). (F) Same as (E), but the data measured close to hot spots has been added and is circled in black.

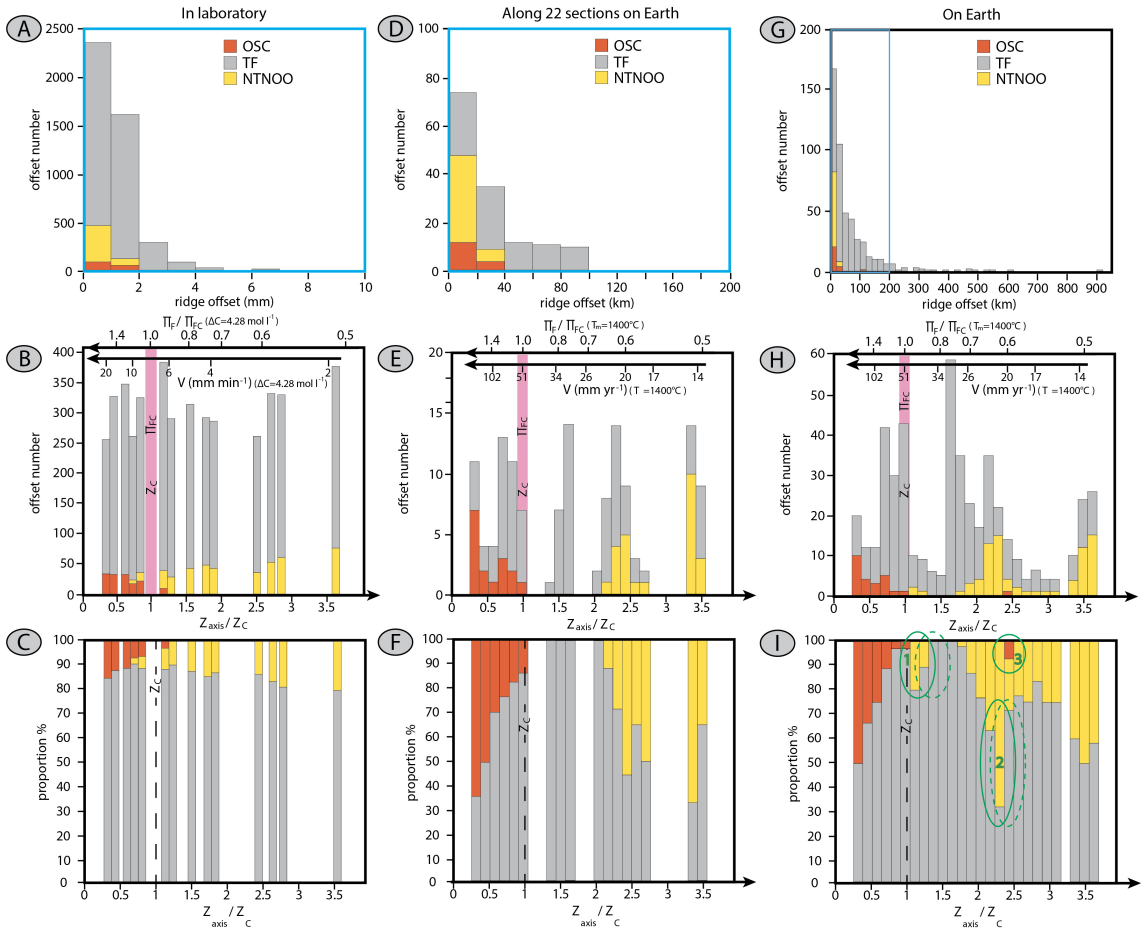

Figure 8: Number of each offset type as a function of their sizes (A, D, G), and as a function of Z_{axis}/Z_c (B, E, H); and (C, F, I) Proportion of each offset type as a function of Z_{axis}/Z_c. Laboratory experiments are shown in (A-C). Earth data for the 22 MOR sections (see text) are shown in (D-F), and for the whole MOR system in (G-I). The blue rectangles indicate the Earth offset range equivalent to the range encountered in the laboratory (see text). The signification of green ellipses are explained in the text.

4. Comparison with the Earth

4.1. Method

As seen in the previous section, in our laboratory experiments only TFs with offsets less than 5 mm develop over the Π_F range relevant to the Earth (Table A2 and Sibrant et al. (2018)). Given the scaling analysis presented in section 2, 5 mm in the laboratory is equivalent to 5mm $\times Z_c(\text{Earth})/Z_c(\text{lab}) \sim 100$ km on Earth. So our experimental results suggest that ridge offsets larger than 100 km on Earth are created by a mechanism that does not exist in our laboratory set-up.

Therefore, to consistently compare laboratory and natural data, we measured segment lengths, and ridge offset types and lateral deviations for all ridge sections: (i) delimited by two ridge offsets larger than 100 km, (ii) with a spreading obliquity less than 15^o, and (iii) with good estimates of spreading velocity and mantle temperature. We measure a total of 22 ridges sections meeting these criteria (fig.7D,E and F), including locations in the Pacific, Indian and Atlantic oceans (Sibrant et al. (2018)). For each ridge section, spreading velocities were taken from the MORVEL model (DeMets et al. (2010)), and mantle temperature from the data-base of Dalton et al (Dalton et al. (2014)).

To compare our analysis with previous studies that examined the entire ridge system (e.g. Schouten et al. (1985); MacDonald et al. (1991); Carbotte et al. (2015)), we also measured the ridge offsets characteristics along the entire ridge system. Ridge offsets were first detected using data from Sandwell and Smith (2009). However, this data set only considered ridge offsets larger than ∼20 km. Therefore, we complemented this first data set by GeoMapApp (Ryan et al. (2009)). Whenever available, we used a mantle temperature value estimated by Dalton et al. (2014) to calculate Z_{axis}; otherwise, we assumed a value of $T_m = 1400^o$C (i.e. the most frequent mantle temperature in Dalton et al. (2014)).

4.2. Statistics

Due to the uneven distribution of plate velocities (fig.2) and, to a lesser degree, of mantle temperature (e.g. Dalton et al. (2014)), statistics on natural data might be difficult to interpret. Since our laboratory experiments provide statistics on the equivalent of a 15,000 km-long MOR for each spreading velocity and mantle temperature considered, we discuss the natural data in light of the trend deduced from the laboratory experiments. Unless otherwise stated, the results concern the data from the 22 MOR sections described above.

Segment length: Fig.7D shows the distribution of segment lengths between two discontinuities of any type. The dispersion appears to increase with decreasing Z_{axis}/Z_c, e.g. increasing spreading velocities or mantle temperature. For $Z_{axis}/Z_c > 1$ (low spreading rates), the mean segment length is approximately constant with a value similar to the one predicted by our experimental scaling: $L_m(\text{Earth}) = L_m(\text{lab}) \times Z_c(\text{Earth})/Z_c(\text{lab}) = 58.7$ km. For $Z_{axis}/Z_c < 1$, the data suggest two trends, with a lower trend that would also be consistent with the same constant L_m value. These natural data would be compatible with a constant mean segment length over the whole MOR spreading range. Moreover, the maximum segment length over the whole MOR system reaches a value of 310 ± 6 km. This value corresponds to 15.73 mm in the laboratory (Table A3), which is in good agreement with the longest segment measured in the experiments (14.6 ± 0.3 mm).

Offset lateral deviation: Away from hotspot influence, natural data present the same behavior as found in laboratory data (fig.7E and B). For $Z_{axis}/Z_c < 1$, natural ridge offset lateral deviation is relatively constant, around 12 km. For $Z_{axis}/Z_c > 1$, the offset lateral deviation increases with increasing Z_{axis}. This offset size increase is well predicted by the elastic fracture mechanics model developed in section 3.4 for the laboratory data. Given the mechanical properties of basalt (Table A1), the Griffiths' length on Earth is L_G=0.2 m. Equation (4) then fits the natural data well (R=0.98854; fig.7E). However, data close to hotspots fall away from the predicted trend, even when Z_{axis} is corrected for a higher mantle temperature (fig.7F).

Offset type: Fig.8 shows that TFs form for all Z_{axis}/Z_c values, i.e. regardless of spreading rate and mantle temperature, while the development of NTNOO and OSC depends on Z_{axis}/Z_c. As observed in the laboratory, the transition between NTNOOs and OSCs occurs around $Z_{axis}/Z_c = 1$ (fig.7E).

Although we cannot directly compare the absolute numbers of ridge offsets on Earth and in the laboratory, it is possible to compare the proportion of OSCs and NTNOOs relative to TFs, for a given Z_{axis}/Z_c ratio (fig.8C,F and I), with the caveat that some spreading rates on Earth are

under-represented (fig.2A). Statistically, TFs are much more numerous than NTNOO or OSC, on Earth and in the laboratory. The main difference between laboratory and natural cases remains in the proportion: NTNOOs constitute up to 20% and up to 50% of the discontinuities, respectively. However, as in the laboratory, the proportion between NTNOO/TF and OSC/TF evolves with Z_{axis}/Z_c. The proportion of TFs relative to OSCs increases with increasing Z_{axis}/Z_c, until $Z_{axis}/Z_c \sim 1$. Then, when $Z_{axis}/Z_c > 1$, the proportion of TFs globally decreases with increasing Z_{axis}/Z_C. The complete absence of NTNOO on Earth for $1 < Z_{axis}/Z_c < 2$ may be due to the paucity of MOR natural data in this range (fig.2A).

If we consider the whole MOR system, only a few MOR sections fall out of the general trend. The South Iceland Seismic Zone (ellipse (3) on fig.8I) is complicated: due to the hotspot, the ridge axis becomes sub-aerial and the Eastern Volcanic Zone in south Iceland is propagating southward. If this region is interpreted as an OSC (Gudmundsson and Brynjolfsson (1993)), it will be the only one developing at Z_{axis}/Z_c >1 (ellipse (3) on fig.8I). However, it has also been interpreted as overlapping propagating rifts (e.g. Schilling et al. (1982); Karson (2017)) or a microplate (e.g. Foulger (2006); Einarsson (2008)). Clearly, the influence of a plume is more complicated than what can be expected from an elevated axial temperature alone.

The Central Indian Ridge (CIR) close to the Rodriguez triple junction (solid ellipse (1) on fig.8I) and the Mid-Atlantic Ridge (MAR) near 37^oN (solid ellipse (2) on fig.8I) are characterized by a significant spreading obliquity $\theta \sim 17^o$ relative to the strike of each segment (Mendel et al. (2000); MacDonald and Luyendyk (1977)). Obliquity reduces the magnitude of the spreading velocity perpendicular to the axis by a factor $cos\theta$ (e.g. Montesi and Behn (2007)). If we take this reduction in spreading rate into account when calculating Z_{axis}, these CIR and MAR data would plot at larger Z_{axis}/Z_c (dashed ellipses on fig.8I). However, it is not sufficient for them to become coherent with the general trend.This suggests that the role of obliquity is more complex. It will be studied in another set of experiments.

4.3. Discussion

Some aspects of MOR segmentation may be inherited from continental breakup (e.g. Wilson (1965)). However, in our experiments, TFs, OSCs and NTNOOs develop from a straight axis. Thus, our results suggest that TFs , OSCs, and NTNOOs are inherent mechanical instabilities of the MOR axis and do not require pre-existing weaknesses and/or inheritance from continental breakup to develop. The laboratory experiments therefore confirm what had been inferred from the development of a crenelated segmentation out of a straight segment South of the Mendocino fracture zone in the late cretaceous (Winterer (1976); Menard (1984)).

Transforms faults: We do not observe TF offsets larger than 5 mm in the laboratory, which corresponds to $\sim$ 100 km on Earth (section 3). Although most of Earth's TFs belong to this category, several TFs on Earth have much larger offsets. It has been suggested that the amplitude of TF offsets on Earth might depend on TF weakness (e.g. Stoddard (1992)). Indeed Earth's TFs are very weak when sheared (Phipps Morgan and Parmentier (1984); Behn et al. (2002)). In numerical simulations, TFs develop only if strong weakening of the material within the TF is implemented (e.g. Choi et al. (2008); Gerya (2010); Allken et al. (2012); Puthe and Gerya (2014)). We observe similar behavior in our experiments where the TF's plane is constituted of a nano-film of water in-between the edges of the solid plates. One could argue that given our experimental setup (fig.3A), any fault is continuously exposed to salted water, and therefore can heal through the action of salt on the silica nanoparticles (Trompette and Meireles (2003)). As healing strongly depends on exposure time to salt, TFs offsets should therefore be shorter at small spreading rates (small Π_F and $Z_{axis}/Z_c > 1$) than at large spreading rates. This is opposite to the trend we observe (fig.7C). So healing does not control the maximum lateral deviation of TF's offsets in the laboratory, and it probably does not control the class of TF with offsets smaller than 100 km on Earth either. Other TFs with much larger offsets, such as Romanche in the Atlantic Ocean, may be inherited from the geometry of initial plate fracturing during continental breakup, i.e. a mechanism that is not documented in our experimental set-up with an initially straight axis.

The absence of TFs at large spreading rates in the Pacific proposed by Naar and Hey (Naar and Hey (1989)) is not supported by the statistics of our experiments (fig.8). The discrepancy between the experiments and the Pacific is probably due to the bias introduced by the uneven distribution of plate velocities on Earth (fig.2). On the other

hand, the absence of TFs at the very small natural spreading rates does not suffer the same bias (fig.2) and, hence, should be recovered in the experimental data. However, although the proportion of TFs decreases with decreasing Π_F (i.e. spreading rate), it does not reach zero within the range of the experiments. Extrapolation of the experimental trend shows that a zero-value would be reached for Z_{axis}/Z_c ∼13. So far, to predict the characteristics of natural ridges from our lab experiments, we have been using the mechanical properties of basaltic crust and assuming that they were independent of the spreading rates or temperature to predict the characteristics of natural ridges from our lab experiments. These values give Z_{axis}/Z_c ∼3.5 for the Earth at ultra-slow spreading rates (e.g. 12 mm/yr). Ultra-slow spreading ridges present a succession of magmatic and amagmatic segments where the crust is extremely thin or absent (Dick et al. (2003)), and the material along the axis is predominantly peridotite. The latter has different mechanical properties. In particular, its tensile strength strongly depends on serpentinization and is much larger than basalt's (e.g. van Noort et al. (2017)). This will increase the Z_{axis}/Z_c beyond its critical value (∼13), and fig.9 shows that indeed TFs could probably not develop in a serpentinized peridotite.

Controls on segmentation: Regardless of the segmentation type (TF, OSC, NTNOO), the scalings we developed from the laboratory data only involve fracture mechanics and advection-diffusion of temperature/salinity. This suggest that the typical length scales of segmentation observed both in the laboratory and on Earth (once the long TFs are excluded) are primarily governed by fracture mechanics. Therefore, melt would move according to the stress field resulting from the segmentation. This is especially true for the ridges where $\Pi_F < \Pi_{Fc}$ (e.g. "tectonic regime", section 3.4). For $\Pi_F > \Pi_{Fc}$, the offset lateral size becomes constant, which could be due to the interaction between melt injection, the structure of the axis, and the stress field. Indeed, in such fast-spreading or high magma supply ridge segments (i.e high Π_F), along-axis crustal thickness is approximately constant, requiring buoyant mantle upwelling (Reid and Jackson (1981); Parmentier and Phipps Morgan (1990)). Upwellings could result from Rayleigh-Taylor-type instabilities of a low-viscosity melt-rich region that underlies the ridge axis (Whitehead et al. (1984); Schouten et al. (1985); Kerr and Lister (1988); Parmentier

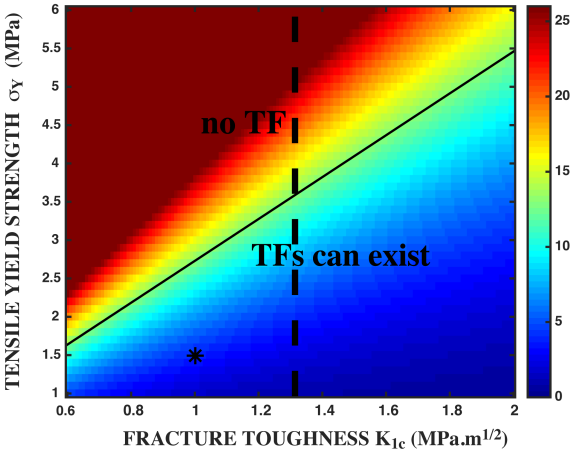

Figure 9: Z_{axis}/Z_c for a very slow spreading ridge like SWIR or Carlsberg as a function of K_{1c} and σ_Y showing the domain of existence of TFs ($Z_{axis}/Z_c < 13$ below the solid black line). For peridotite in water, $K_{1c} \sim 1.3$ MPa.m$^{1/2}$ (e.g. Hao et al. (2015)); it corresponds to the dashed black line. Tensile strength of fresh peridotite ranges between 50 and 280 MPa (He et al. (1995)); while for serpentinized peridotite, it ranges between 2 and 50 MPa (e.g. van Noort et al. (2017)). The star symbol shows the properties of basalt.

.

and Phipps Morgan (1990); Lin and Phipps Morgan (1992); Sarkar et al. (2014); Mandal et al. (2018)) or from small-scale convection in the asthenosphere below the axis (Rabinowicz et al. (1993); Sparks et al. (1993); Rouzo et al. (1995); Briais and Rabinowicz (2002)). Upwelling spacing could range from ∼20 km for melt channeling through a crystallizing porous media (Sarkar et al. (2014); Mandal et al. (2018)) to 100-300 km for asthenospheric convection (Parmentier and Phipps Morgan (1990); Rouzo et al. (1995); Sparks et al. (1993)). These estimates are, respectively, smaller and larger than the ∼55 km average ridge segment length observed on natural data (Carbotte et al. (2015)) and predicted by our experimental scaling. The higher range might explain the appearance of a second trend in the segment length natural data at large spreading velocity (fig.7D), unless this trend is again the result of a small number bias (fig.2). On the other hand, seismic observations (Toomey et al. (2007); Vanderbeek et al. (2016)) suggest that reorientation of segments and formation of new ridge discontinuities could result from mantle flow oblique to the ridge axis. We do not observe any coherent, large-scale circulation in our experimental mantle. However, we do observe small-scale convection beneath the lithosphere (Sibrant et al. (2018)). Although this

small-scale convection does not seem to originate below the axis, the effect on the flow under the ridge is currently impossible to quantify. So whether the observed pattern of segmentation formed by mechanical instabilities of the ridge axis also requires an active contribution from mantle flow remains an open question.

5. Conclusions

Based on experimental modelling, we study the segmentation characteristics and offset types of mid-ocean ridges for a constant, symmetric spreading velocity initially perpendicular to the spreading axis. We show that, like the mode of axial failure (tectonic or magmatic) and the overall shape of oceanic ridges (Sibrant et al. (2018)), their segmentation characteristics at a given time depend on a single parameter, the axial failure parameter Π_F, which is the ratio of a length scale depending only on the mechanical properties of the plate boundary and the axial elastic thickness, which depends on mantle temperature and spreading velocity. Scaling laws derived from the experimental data and fracture mechanics modeling suggest that on Earth, short TFs (offset < 100 km) , OSCs, and NTNOOs appear to be inherent mechanical instabilities of the MOR axis. They do not require inheritance from plate break-up to develop. Moreover, the typical length scales of ridge segmentation seem primarily governed by fracture mechanics regardless of spreading rate, while the role of upwelling melt and mantle flow could increase with spreading rate. The present study focussed on snapshots of the ridges; more work is now underway to characterize the time-evolution of MOR morphology and of the different types of segmentation, as well as the influence of ridge obliquity.

Acknowledgments: This study benefited from funding by the French CNRS-INSU-CNES program PNP-SEDIT, the French ANR (project PTECTO) and LabEx PALM (ANR-10-LABX-0039-PALM). A. Sibrant was supported by the NSF under the EAR GeoPRISMS programme (grant no.EAR-1456664) and by an international post-doctoral grant of the Laboratoire d'Excellence LabexMER. E. Mittelstaedt was supported by NSF grant OCE-1753354. The manuscript was improved thanks to the comments of Taras Gerya and an anonymous reviewer.

Appendix A. Tables and Supplementary figure

References

Allain, C., Limat, L., 1995. Regular patterns of cracks formed by directional drying of a collodial suspension. Physical Review Letters 74, 2981–2984.

Allken, V., Huismans, R.S., Thieulot, C., 2012. Factors controlling the mode of rift interaction in brittle-ductile coupled systems: A 3d numerical study. Geochem. Geophys. Geosyst. 13, Q05010.

Behn, M.D., Lin, J., Zuber, M.T., 2002. Evidence for weak oceanic transform faults. Geophys. Res. Lett. 24, 2207.

Bonatti, E., Ligi, M., Gasperini, L., Peyve, A., Raznitsin, Y., Chen, Y.J., 1994. Transform migration and vertical tectonics at the romanche fracture zone, equatorial atlantic. J. Geophys. Res. 99, 21779–21802.

Bosworth, W., 1986. Comment on detachment faulting and the evolution of passive continental margins. Geology 14, 890–891.

Briais, A., Rabinowicz, M., 2002. Temporal variations of the segmentation of slow to intermediate spreading mid-ocean ridges. 1. synoptic observations based on satellite altimetry data. J. Geophys. Res. 107, 2098.

Buck, W.R., Lavier, L.L., Poliakov, A.N.B., 2005. Modes of faulting at mid- ocean ridges. Nature 434, 719–723.

Carbotte, S.M., Smith, D.K., Cannat, M., Klein, E.M., 2015. Tectonic and magmatic segmentation of the global ocean ridge system : a synthe- sis of observations. Geological Society of London, Special Publications 420.

Chen, Y., Morgan, W.J., 1190. Rift valley/no rift valley transition at mid- ocean ridges. J. Geophys. Res. 95, 17571–17581.

Choi, E.S., Lavier, L., Gurnis, M., 2008. Thermomechanics of mid-ocean ridge segmentation. Phys. Earth Planet. Int. 171, 374–386.

Cochran, J., Sempere, J.C., 1997. The southeast indian ridge between 88e and 118e: gravity anomalies and crustal accretion at intermediate spreading rates. J. Geophys. Res. 102, 15463–15487.

Dalton, C.A., Langmuir, C.H., Gale, A., 2014. Geophysical and geochemical evidence for deep temperature variations beneath mid-ocean ridges. Science 344, 80.

DeMets, C., Gordon, R.G., Argus, D.F., 2010. Geologically current plate motions. Geophys. J. Int. 181, 1–80.

Di Giuseppe, E., Davaille, A., Mittelstaedt, E., Francois, M., 2012. Rheological and mechanical properties of silica colloids: from newtonian liquid to brittle behavior. Rheologica Acta 51, 451–465.

Dick, H.J.B., Lin, J., Schouten, H., 2003. An ultraslow-spreading class of ocean ridge. Nature 426, 405–412.

Einarsson, P., 2008. Plate boundaries, rifts and transforms in iceland. Jokull 58, 35–58.

Foulger, G.R., 2006. Older crust underlies iceland. Geophys. J. Int. 165, 672–676.

Gauthier, G., Lazarus, V., Pauchard, L., 2010. Shrinkage star-shaped cracks: Explaining the transition from 90 degrees to 120 degrees. EPL .

Gerya, T., 2010. Dynamical instability produces transform faults at mid-ocean ridges. Science 329, 1047–1050.

Griffith, A.A., 1924. The phenomena of rupture and flow in solids. Philos. Trans. R. Soc. London 221, 163–198.

Table A.1: Physical and mechanical properties. (a) Di Giuseppe et al. (2012) (b) Turcotte and Schubert (2002); (c) Kohlstedt et al. (1995); (d) Vah and Davaille (in prep.); (e) Sibrant et al. (2018); (f) Schultz (1993).

Property	Colloidal dispersion	Earth
Density (ρ)	1295 kg/m$^{3(a)}$	3000 kg/m$^{3(b)}$
Asthenosphere viscosity (η)	17 10^{-3} Pa.s $^{(a)}$	10^{19} Pa.s $^{(c)}$
Diffusivity (κ)	1.6 10^{-9} m^2/s $^{(d)}$	10^{-6} m^2/s $^{(b)}$
Poisson ratio (ν_P)	0.3 $^{(e)}$	0.25 to 0.3 $^{(f)}$
Tensile yield strength (σ_Y)	14 $\pm$ 2 MPa $^{(e)}$	1.5 MPa $^{(f)}$
Fracture toughness (K_{1c})	2.1 $\pm$ 0.3 kPa.m$^{1/2}(e)$	1 MPa.m $^{1/2(f)}$

Table A.2: Experimental parameters. V is the full spreading rate. The solid line separates the experiments with $\Pi_F > \Pi_{Fc}$ on top of the table, from experiments with $\Pi_F < \Pi_{Fc}$.

run	ΔC_0 (mol/l)	V (mm/min)	Π_F	Pe
HS40-33	4.28	20	3.90 10^{-2}	1562
HS40-52	2.79	12	3.56 10^{-2}	937
HS40-50	2.79	8	2.91 10^{-2}	625
HS40-32	4.28	10	2.76 10^{-2}	781
HS40-58	6.15	12	2.72 10^{-2}	469
HS40-61	4.12	6	2.17 10^{-2}	469
HS40-29	4.28	6	2.14 10^{-2}	469
HS40-57	6.15	6	1.92 10^{-2}	937
HS40-43	2.79	3	1.78 10^{-2}	234
HS40-30	4.28	4	1.75 10^{-2}	312
HS40-34	4.28	3	1.51 10^{-2}	234
HS40-80	4.91	3	1.45 10^{-2}	234
HS40-21	3.00	2	1.41 10^{-2}	156
HS40-14	4.28	2	1.23 10^{-2}	156

Table A.3: Experimental results. Data listed for each experiment include the calculated axis elastic thickness Z_{axis}, the average offset lateral deviation d_l, its maximum value and the latter corresponding value for the Earth. the average segment length L_m, its standard deviation, its maximum value and the latter corresponding value for the Earth. The solid line separates the experiments with $\Pi_F > \Pi_{Fc}$ on top of the table, from experiments with $\Pi_F < \Pi_{Fc}$.

run	Z_{axis} (μm)	mean(d_l) (mm)	std(d_l) (mm)	max(d_l) (mm)	Earth (km)	mean(L_m) (mm)	std(L_m) (mm)	max(L_m) (mm)	Earth (km)
HS40-33	14.8	0.57	0.32	4.25	83.7	2.87	1.55	11.8	236
HS40-52	17.8	0.56	0.29	4.80	94.5	2.80	1.79	13.24	265
HS40-50	26.6	0.55	0.27	3.56	70.1	2.64	1.47	11.3	226
HS40-32	29.5	0.60	0.37	4.48	88.3	3.02	2.15	11.0	220
HS40-58	30.4	0.59	0.31	4.27	84.1	2.73	1.77	14.4	288
HS40-61	48.0	0.64	0.31	3.48	68.5	2.66	1.22	13.32	266
HS40-29	49.2	0.67	0.38	4.50	88.6	2.77	1.95	12.33	246
HS40-57	60.8	0.78	0.40	4.34	85.5	2.92	1.27	9.72	194
HS40-43	71.0	0.77	0.33	4.25	83.7	2.83	1.28	14.6	292
HS40-30	73.8	0.81	0.42	4.14	81.5	2.84	1.17	11.82	236
HS40-34	98.4	0.94	0.52	4.26	83.9	2.95	2.14	12.21	244
HS40-80	107	0.99	0.42	4.53	89.2	2.74	1.15	11.28	225
HS40-21	113	1.04	0.34	3.95	77.8	2.68	1.05	10.62	212
HS40-14	148	1.15	0.36	4.75	93.56	2.50	1.08	10.3	206

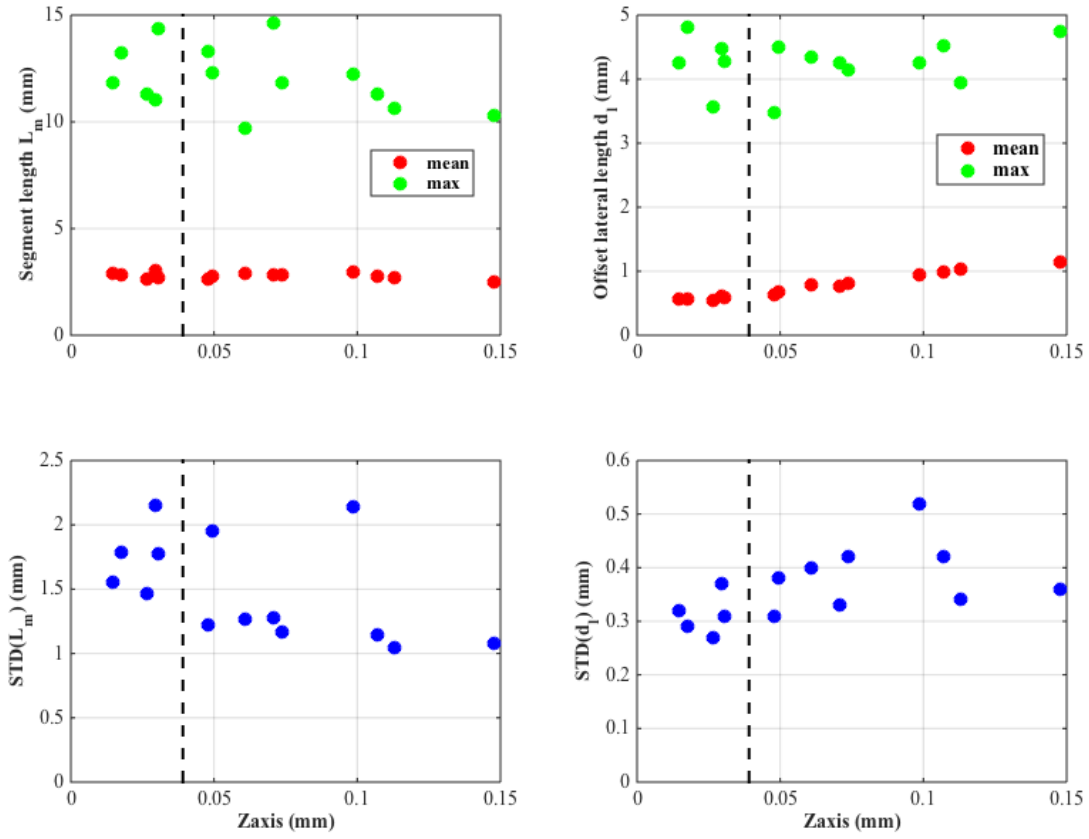

Figure A.10: Experimental data as a function of the axial elastic thickness. The black dashed line corresponds to $\Pi_F = \Pi_{Fc}$. STD stands for standard deviation. For each experiment, the average value of segment length and of offset size are in red, while their maximum values are in green.

Gudmundsson, A., Brynjolfsson, S., 1993. Overlapping rift-zone segments and the evolution of the south iceland seismic zone. Geophys. Res. Lett. 20, 1903–1906.

Hao, R., Li, J., Cao, P., Liu, B., Liao, J., 2015. Test of subcritical crack growth and fracture toughness under water-rock interaction in three types of rocks. J. Cent. South Univ. 22, 662–668.

He, H., Jin, S., Jing, F., Ahrens, T., 1995. Characteristic of dynamic tensile fracture in augite-peridotite. Shock Compression of Condensed Matter, AIP Press, New York, NY, USA.

Hey, R., 1977. A new class of "pseudofaults" and their bearing on plate tectonics: a propagating rift model. Earth Planet. Sci. Lett. 37, 321–325.

Houseman, G., 1983. The deep structure of ocean ridges in a convecting mantle. Earth Planet. Sci. Lett. 64, 283–294.

Howell, S.M., Olive, J.A., Ito, G., Behn, M.D., Escartin, J., Kaus, B., 2019. Seafloor expression of oceanic detachment faulting reflects gradients in mid-ocean ridge magma supply. Earth Planet. Sci. Lett. 516, 176–189.

Ito, G., Shen, Y., Hirth, G., Wolfe, C., 1999. Mantle flow, melting and dehydratation of the iceland mantle plume. Earth Planet. Sci. Lett. 165, 81–96.

Karson, J.A., 2017. The iceland plate boundary zone: propagating rifts, migrating transforms, and rift-parallel strike-slip faults. Geochemistry, Geophysics, Geosystems 18, 4043–4054.

Kerr, R., Lister, J.R., 1988. Island arc and mid-ocean ridge volcanism, modelled by diapirism from linear source regions. Earth Planet. Sci. Lett. 88, 143–152.

Kohlstedt, D.L., Evans, B., Mackwell, S.J., 1995. Strength of the lithosphere: Constraints imposed by laboratory experiments. J. Geophys. Res. 100, 17587–17602.

Langmuir, C.H., Bender, J.F., Batiza, R., 1986. Petrological and tectonic segmentation of the east pacific rise, 5 °30' - 14 °30' n. Nature 322, 422–429.

Lin, J., Phipps Morgan, J., 1992. The spreading rate dependence of threedimensional midocean ridge gravity structure. Geophys. Res. Lett. 19, 13–16.

Lonsdale, P., 1983. Overlapping rift zones at the 5.5 s offset of the east pacific rise. J. Geophys. Res. 88, 9393–9406.

MacDonald, K.C., 1982. Mid-ocean ridges: Fine-scale tectonic, volcanic and hydrothermal processes within the plate boundary zone. Annual Review of Earth and Planetary Sciences 10, 155–190.

MacDonald, K.C., Fox, P.J., 1983. Overlapping spreading centers: New accretion geometry on the east pacific rise. Nature 302, 55–58.

MacDonald, K.C., Fox, P.J., 1992. The east pacific rise and its flanks 8-18 °n: history of segmentation, propagation and spreading direction based on seamarc ii and sea beam studies. Marine Geophysical Research 14, 299–344.

Macdonald, K.C., Fox, P.J., et al, 1988. A new view of the mid-ocean ridge from the behavior of ridge-axis discontinuities. Nature 335, 217–225.

MacDonald, K.C., Luyendyk, B.P., 1977. Deep-tow studies of the structure of the mid-atlantic ridge crest near lat. 37 °n. Geol. Soc. Am. Bull. 88, 621–636.

MacDonald, K.C., Scheirer, D.S., Carbotte, S.M., 1991. Mid-ocean ridges: Discontinuities, segments and giant cracks. Science 253, 986–994.

Mandal, N., Sarkar, S., Baruah, A., Dutta, U., 2018. Production, pathways and budgets of melts in mid-ocean ridges: An enthalpy based thermo-mechanical model. Phys. Earth Planet. Int. 277, 55–69.

McKenzie, D., Jackson, J., Priestley, K., 2005. Thermal structure of oceanic and continental lithosphere. Earth Planet. Sci. Lett. 233, 337–349.

Menard, H., 1984. Evolution of ridges by asymmetrical spreading. Geology 12, 177–180.

Mendel, V., Sauter, D., Munschy, M., 2000. Relationship of the central indian ridge segmentation with the evolution of the rodrigues triple junction for the past 8 myr. J. Geophys. Res. 105, 16563–16575.

Mjelde, R., Breivik, A.J., Raum, T., Mittelstaedt, E., Ito, G., Faleide, J.I., 2008. Magmatic and tectonic evolution of the north atlantic. J. Geol. Soc. 165, 31–42.

Montesi, L.G.J., Behn, M.D., 2007. Mantle flow and melting underneath oblique and ultraslow mid-ocean ridges. Geophys. Res. Lett. 34.

Naar, D.F., Hey, R.N., 1989. Speed limit for oceanic transform faults. Geology 17, 420–422.

van Noort, R., Wolterbeek, T.K.T., Drury, M.R., Kandianis, M.T., Spiers, C.J., 2017. The force of crystallization and fracture propagation during in-situ carbonation of peridotite. Minerals 7, 190.

Parmentier, E.M., Phipps Morgan, J., 1990. Spreading rate dependence of three-dimensional structure in oceanic spreading centres. Nature 348, 325–328.

Phipps Morgan, J., Parmentier, E., 1984. Lithospheric stress near a ridge transform intersection. J. Geophys. Res. 11, 113–116.

Phipps Morgan, J., Parmentier, E.M., Lin, J., 1987. Mechanisms for the origin of mid-ocean ridge axial topography: Implications for the thermal and mechanical structure of accreting plate boundaries. J. Geophys. Res. 92, 12823–12836.

Puthe, C., Gerya, T.V., 2014. Dependence of mid-ocean ridge morphology on spreading rate in numerical 3-d models. Gondwana Research 25, 270–283.

Rabinowicz, M., Rouzo, S., Sempere, J.C., Rosemberg, C., 1993. Three-dimensional mantle flow beneath mid-ocean ridges. J. Geophys. Res. 98, 7851–7869.

Reid, I., Jackson, H.R., 1981. Oceanic spreading rate and crustal thickness. Marine Geophysical Researches 5, 165–172.

Rouzo, S., Rabinowicz, M., Briais, A., 1995. Segmentation of mid-ocean ridges with an axial valley induced by small-scale convection. Nature 374, 795–798.

Ryan, W., Carbotte, S., Coplan, J., O'Hara, S., Melkonian, A., Arko, R., Weissel, R., Ferrini, V., Goodwillie, A., Nitsche, F., Bonczkowski, J., Zemsky, R., 2009. The global multi-resolution topography synthesis. Geochem. Geophys. Geosyst. 10.

Sandwell, D.T., 1986. Thermal stress and the spacings of transform faults. J. Geophys. Res. 91, 6405–6417.

Sarkar, S., Baruah, A., Dutta, U., Mandal, N., 2014. Role of random thermal perturbations in the magmatic segmentation of mid-oceanic ridges: Insights from numerical simulations. Tectonophysics 636, 83–99.

Schilling, J.G., Meyer, P., Kingsley, R., 1982. Evolution of the iceland hotpost. Nature 296, 313–320.

Schouten, H., Dick, H.J.B., Klitgord, K.D., 1987. Migration of mid-ocean-ridge volcanic segments. Nature 326, 835–839.

Schouten, H., Klitgord, K.D., 1982. The memory of the accreting plate boundary and the continuity of fracture zones. Earth Planet. Sci. Lett. 59, 255–266.

Schouten, H., Klitgord, K.D., Whitehead, J.A., 1985. Segmentation of mid-ocean ridges. Nature 317, 225–229.

Schouten, H., White, R.S., 1980. Zero-offset fracture zones. Geology 8, 175–179.

Schultz, R.A., 1993. Brittle strength of basaltic rock masses with applications to venus. J. Geophys. Res. 98, 10883–10895.

Sempere, J.C., Lin, J., Brown, H.S., Schouten, H., Purdy, G.M., 1993. Segmentation and morphotectonic variations along a slow-spreading center: the mid-atlantic ridge (24 °00'n - 30 °40'n). Marine Geophysical Research 15, 153–200.

Sempere, J.C., Palmer, J., Christies, D., Phipps Morgan, J., Shor, A., 1991. The australian-antartic discordance. Geology 19, 429–432.

Shih, W.Y., Shih, W.H., Aksay, I.A., 1999. Elastic and yield behavior of strongly flocculated colloids. J. Am. Ceram. Soc. 82, 616–624.

Sibrant, A.L.R., Pauchard, L., 2016. Effect of the particle interactions on the structuration and mechanical strength of particulate materials. EPL 116.

Sibrant, A.R.L., Mittelstaedt, E., Davaille, A., Pauchard, L., Aubertin, A., Auffray, L., Pidoux, R., 2018. Accretion mode of oceanic ridges governed by axial mechanical strength. Nature Geosciences 11, 274–279.

Sparks, D.W., Parmentier, E., Phipps Morgan, J., 1993. Three-dimensional mantle convection beneath a segmented spreading center: Implications for along-axis variations in crustal thickness and gravity. J. Geophys. Res. 98, 21977–21995.

Stoddard, P.R., 1992. On the relation between transform fault resistance and plate motion. J. Geophys. Res. 97, 17637–17650.

Toomey, D.R., Jousselin, D., Dunn, R.A., Wilcock, W.S.D., Detrick, R.S., 2007. Skew of mantle upwelling beneath the east pacific rise governs segmentation. Nature 446, 409–414.

Trompette, J.L., Meireles, M., 2003. Ion-specific effect on the gelation kinetics of concentrated colloidal silica suspensions. J. Colloid Interface Sci. 263, 522–527.

Turcotte, D., Schubert, G., 2002. Geodynamics. Second ed. ed., Cambridge University Press.

Vanderbeek, B., Toomey, D.R., Hooft, E., Wilcock, W., 2016. Segmentation of mid-ocean ridges attributed to oblique mantle divergence. Nature Geosciences 9, 636–642.

Whitehead, J.A., Dick, H.J., Schouten, H., 1984. A mechanism for magmatic accretion under spreading centres. Nature 312, 146–148.

Wilson, J.T., 1965. A new class of faults and their bearing on continental drift. Nature 207, 343–347.

Winterer, E., 1976. Anomalies in the tectonic evolution of the pacific, in: Sutton, G., Manghnani, M., Moberty, R. (Eds.), The geophysics fo the Pacific Ocean basin and its margin. AGU. volume 19 of *Geophys. Monogr. Ser.*, pp. 269–280.